

Article

Industrial Rotary Kiln Burner Performance with 3D CFD Modeling

Duarte M. Cecílio ^{1,2,*}, Margarida Mateus ^{1,2}  and Ana Isabel Ferreiro ^{1,3} 

¹ Secil S.A., Fábrica Secil, Estrada do Outão, 2901-864 Setúbal, Portugal; margarida.mateus@tecnico.ulisboa.pt (M.M.); isabel.ferreiro@secil.pt (A.I.F.)

² CERENA—Centro de Recursos Naturais e Ambiente, Departamento de Engenharia Química, Instituto Superior Técnico, Universidade de Lisboa, 1049-001 Lisboa, Portugal

³ IDMEC—Instituto de Engenharia Mecânica, Instituto Superior Técnico, Universidade de Lisboa, 1049-001 Lisboa, Portugal

* Correspondence: duarte.cecilio@secil.pt

Abstract: As the need to minimize environmental impacts continues to rise, it is essential to incorporate, advance, and adopt renewable energy sources and materials to attain climate neutrality in industrial operations. It is established that economic growth is built upon infrastructure, where the cement industry plays a crucial role. However, it is also known that this industry is actively looking for ways to transition toward low-carbon practices to encourage sustainable and environmentally conscious practices. To this end, the use of refuse-derived fuels to substitute fossil fuels is very appealing, as these have the potential to lower clinker production costs and CO₂ emissions. Bearing this in mind, the primary objective of this work is to gain insights into the combustion behavior in an industrial rotary kiln by studying real-life scenarios and to assess the potential of substituting alternative fuels for fossil fuels to reduce CO₂ emissions. A 3D CFD turbulent combustion model was formulated in Ansys® considering a Pillard NOVAFLAM® burner, where refuse-derived and petcoke fuels were used, and different secondary air mass flows were considered. From the obtained results, it was possible to conclude that the outcome of the combustion process is greatly influenced by the fuel-to-air ratio. Increasing the secondary air mass flow promotes the occurrence of a complete and efficient combustion process, leading to enhanced fuel conversion and the decreased formation of pollutants such as CO, soot, and unburned hydrocarbons. An increase in combustion efficiency from 93% to 96% was observed, coupled with a slight decrease in the pollutant mass fraction in the flue gas.

Keywords: CFD; combustion; alternative fuels; burners; clinkerization; CO₂



Citation: Cecílio, D.M.; Mateus, M.; Ferreiro, A.I. Industrial Rotary Kiln Burner Performance with 3D CFD Modeling. *Fuels* **2023**, *4*, 454–468. <https://doi.org/10.3390/fuels4040028>

Academic Editor: Sarma V. Pisupati

Received: 8 August 2023

Revised: 6 September 2023

Accepted: 18 September 2023

Published: 2 November 2023



Copyright: © 2023 by the authors. Licensee MDPI, Basel, Switzerland. This article is an open access article distributed under the terms and conditions of the Creative Commons Attribution (CC BY) license (<https://creativecommons.org/licenses/by/4.0/>).

1. Introduction

The current global population and technological advancements have created a pressing need for a sustainable society, where the green economy plays a key role [1]. In response to the growing demand for reducing environmental impacts, it has become imperative to integrate, innovate, and embrace renewable sources of energy and materials to achieve climate neutrality. Achieving climate neutrality means creating a balance between greenhouse gas emissions and their removal, primarily by reducing emissions, advancing sustainable technologies, and preserving natural ecosystems [2]. Since the foundation of economic growth is built upon infrastructure, the cement industry plays a crucial role here [1]. However, producing cement clinker is energetically intensive and significantly contributes to CO₂ emissions worldwide. Nonetheless, it is known that the industry is proactively pursuing ways to transition toward low-carbon practices to promote sustainable and environmentally conscious practices [3,4]. Additionally, the use of refuse-derived fuels (RDF) to substitute fossil fuels is also very appealing in the cement industry, as these have the potential to lower clinker production costs and CO₂ emissions [5–7]. The use of RDF in the cement

industry has actually been a common practice since the 1980s. It was introduced to fight the high costs inherent to the first oil crisis and has been considered an efficient way of boosting industry decarbonization ever since [3].

The increase in waste generation, coupled with the inadequate management strategies currently employed, means that the co-processing of waste as an alternative fuel in cement plants offers significant advantages by avoiding landfills [3,5,8,9]. However, RDF are difficult to handle due to their variable physical and chemical properties, such as density, homogeneity, moisture content, and composition, and, for that reason, can greatly affect the combustion behavior within a cement rotary kiln [3]. For instance, high-density particles tend to exhibit lower suspension capacities in a gas flow, implying changes in their trajectory and residence time in open flames [10]. This behavior can significantly affect particles' burnout, and if a particle is left unburned, it may deposit onto the clinker being produced and reduce its quality [11].

Conducting experiments in industrial facilities can be prohibitively expensive, underlining the extreme importance of modeling to simulate and optimize processes before implementing them in a real-world setting, especially using computational fluid dynamics (CFD) [10–12]. Some authors have used CFD modeling to predict the combustion behavior using alternative fuels in industrial cement rotary kilns in terms of flame temperature, flow velocity, flame stability, fuel and oxidant composition, emissions, and calcination reactions [7,10,11,13,14]. Liedmann et al. [7] started to study the influence of operating conditions in cement rotary kilns by co-firing different mixtures of RDF and pulverized coal. The authors experimentally characterized the different constituents of RDF (2D foils, 3D plastics, paper and cardboard, textiles, and fines) and studied their specific flight paths in an automated drop-shaft to obtain drag and lift coefficients and their corresponding fluctuations. With this preliminary study, the authors concluded that each type of particle fraction had different motion trajectories, especially when compared to those of pulverized coal. Hence, it was stated that this phenomenon should be taken into consideration when modeling combustion. Later, Liedmann et al. [10] continued their research and presented a simplified modeling approach that allows the prediction of the trajectory of each particle fraction and its combustion behavior separately. The authors concluded that the simplified model provided detailed information about each particle fraction trajectory and combustion. In the specific case of substituting 15% of the thermal heat using RDF, a burnout of 83% was observed. Pieper et al. [11] studied the combustion behavior in an industrial rotary cement kiln using a mixture of pulverized coal and RDF. The authors used advanced CFD models to characterize the thermal conversion process of non-spherical RDF particles and complemented this study by coupling a simplified 1-D model to evaluate the heat and mass transfer between the clinker bed and the gas phase within the kiln. The authors concluded that having a mixture of 50% RDF with 50% lignite led to a combustion delay, a temperature increase in the direction of the fuel inlet, and a temperature drop of 45 K in the gas phase in the sintering zone. They also added that larger particles can be projected to the clinker bed or to the kiln walls, showing different burnout behaviors, limiting the conversion degree to 68%. In a later work, Pieper et al. [13] extended their study to predict the locations of regions inside the rotary kiln that exhibit coating layers from both RDF combustion and the clinker phase, i.e., the adhesion of agglomerated particles that can decrease the process efficiency and clinker quality. The authors concluded that coating layers could decrease the residence time and the burnout of RDF particles during the gas phase, thus being deposited unburned in the clinker bed. The authors also stated that interaction mechanisms inside a rotary kiln are substantially more complex and that the validation of these results with plant data is impractical, for obvious reasons. Nevertheless, predictions show good qualitative agreement when comparing them with observations made by cement plant operators. Ariyaratne et al. [14] performed 3D CFD simulations to predict the effect of fuel particle size and feeding on the combustion behavior within an industrial cement rotary kiln. The authors independently modeled different cases with the use of pulverized coal and meat and bone meal (MBM), using different excess air coefficients, fuel feeding rates,

and particle size distributions. The authors concluded that for the same thermal input, when coal is compared with MBM, the gas temperature is lower. This is expected due to the high content of moisture and ashes present in the MBM composition and, as a consequence, slower devolatilization in the flame region. It was also added that combustion is more efficient for smaller particles since a higher burnout is reached.

It is well established that an industrial burner of a cement rotary kiln has different entries to receive primary and alternative fuels in different states of matter [14–17]. Additionally, to achieve self-sustained combustion, different air mass flows must be supplied (commonly primary and preheated secondary air) [15,16]. Based on the information provided above, it is realizable that modeling is usually performed by simplifying the geometry of the burner or the mixture of fuels. Additionally, in most cases, only a 2D CFD turbulent combustion model is provided to describe the functioning inside the rotary kiln, which nonetheless provides significant information. However, in these cases, symmetry conditions are assumed when, in real setups, these do not occur. As a way of contributing to filling this gap, the novelty of the present work is the development of a 3D CFD turbulent combustion model based on real industrial data, considering a Pillard NOVAFLAM[®] burner type, with multiple entries for different fuels and multiple entries for the primary and secondary air, including swirl. The model was formulated in Ansys Fluent[®] version 2022 R2 using a blend of different fuels (petcoke and RDF) and base case scenarios from an industrial cement rotary kiln. The main objectives of this work are to provide valuable knowledge about the combustion behavior occurring within the rotary kiln by studying real case scenarios and to take one step forward and evaluate how far it is possible to go in substituting alternative fuels for fossil fuels to contribute to the mitigation of CO₂ emissions. Predictions will provide information on temperature and velocity fields, flame length, position and temperature, emissions, major species devolatilization, and volatile combustion.

2. Materials and Methods

The fuels used for the simulation and their respective properties are presented in Table 1. These are divided into a fossil fuel (petcoke) and refuse-derived fuel (RDF) as the alternative fuel. Note that all fuel data was obtained from characterization performed at the plant.

Table 1. Properties of the fuels employed in the simulations.

Parameter	Petcoke	RDF
Total moisture (wt. %)	7.7	16.9
Ash (wt. %)	0.7	12.4
Fixed carbon (wt. %)	80.5	11.3
Volatile content (wt. %)	11.1	59.4
Carbon (wt. %)	86.5	62.6
Hydrogen (wt. %)	3.9	8.1
Nitrogen (wt. %)	0.0	1.9
Sulfur (wt. %)	6.2	0.0
Oxygen (wt. %)	3.4	27.4
Lower Heating Value (MJ/kg)	23.00	19.40
Dry density (kg/m ³)	1200	300
Max. diameter (μm)	90	3 × 10 ³
Mean diameter (μm)	40	300
Min. diameter (μm)	10	100

2.1. Kiln Model Geometry and Mesh

Figure 1 shows the geometry of the burner and burner tip. The burner is focused on solid fuel combustion, with an annular inlet for fossil fuels (5), a larger central circular inlet for solid alternative fuels (6), and two smaller inlet nozzles for the igniter and liquid alternative fuels (7). Primary air can be seen through a combination of the outer circular

inlets that feed in the axial air (1), immediately followed by slots where radial air is fed (2). The solid alternative fuel inlet is also surrounded by small nozzles to improve the mixture of air and fuel prior to burning (4). Lastly, several small inlets constitute cooling air to prevent damage to the burner end plate (3).

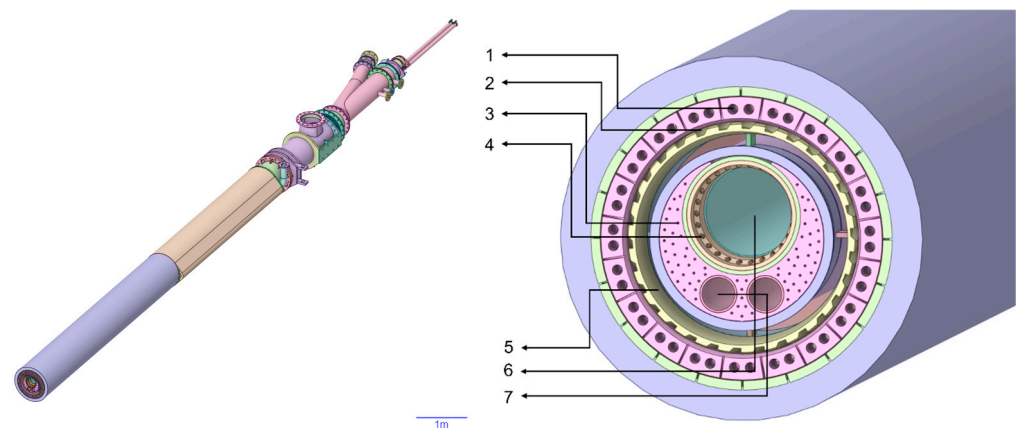


Figure 1. Geometry of the burner (left panel) and burner tip (right panel).

Considering this geometry, the fluid volume within is extracted and combined to produce a continuous solid, depicted in Figure 2. The cooling air nozzles were removed for simplification, as the amount of air injected is insignificant and does not impact the flame shape. Cooling air makes up approximately 1% of primary air and 0.1% of total air, and its function is to cool the burner end plate to prevent the steel from warping. As such, it does not contribute to flame control, and its omission from the geometry significantly reduces the computational complexity associated with the model.

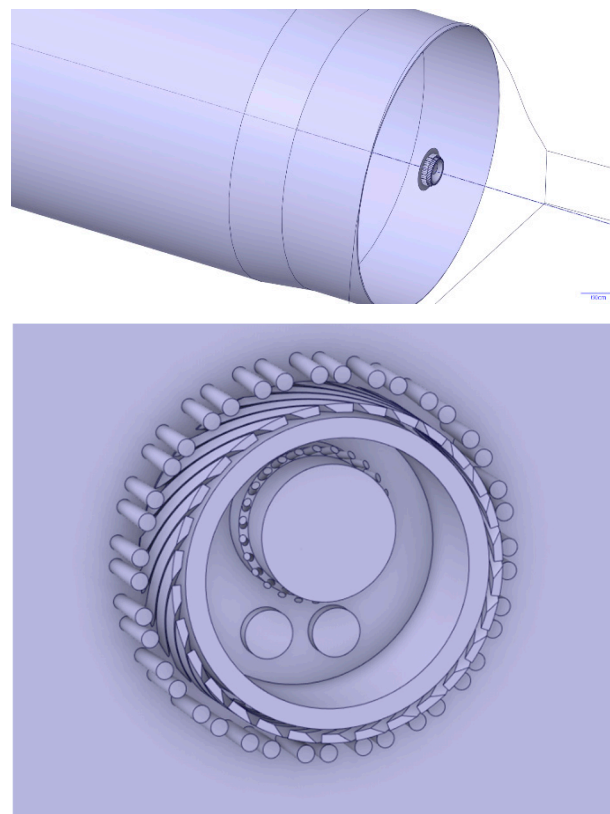


Figure 2. Geometry of the fluid volume for CFD simulation.

Lastly, the kiln and burner geometries were combined with the clinker cooler hood, yielding the final simulated geometry, depicted in Figure 3. In addition to the specified burner inlets, on the right end of the geometry is the clinker cooler hood, where the preheated secondary air enters the system. The hot flue gases resulting from the combustion process then exit the domain at the leftmost boundary of the domain, which represents the boundary between the rotary kiln and the fume hood at the bottom of the preheater tower.

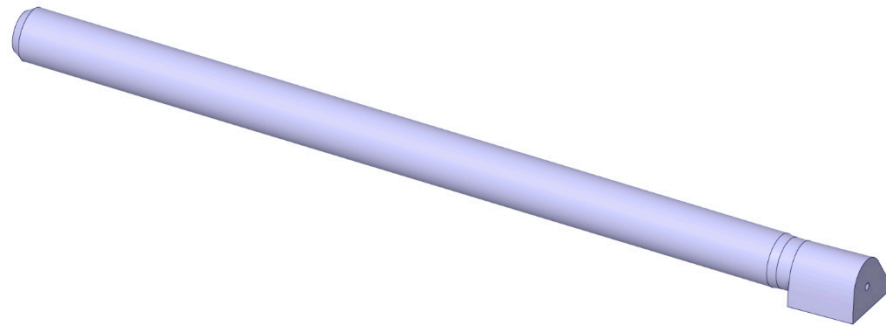


Figure 3. Kiln CFD geometry with clinker cooler hood.

The volume was then discretized into a mesh, depicted in Figure 4.

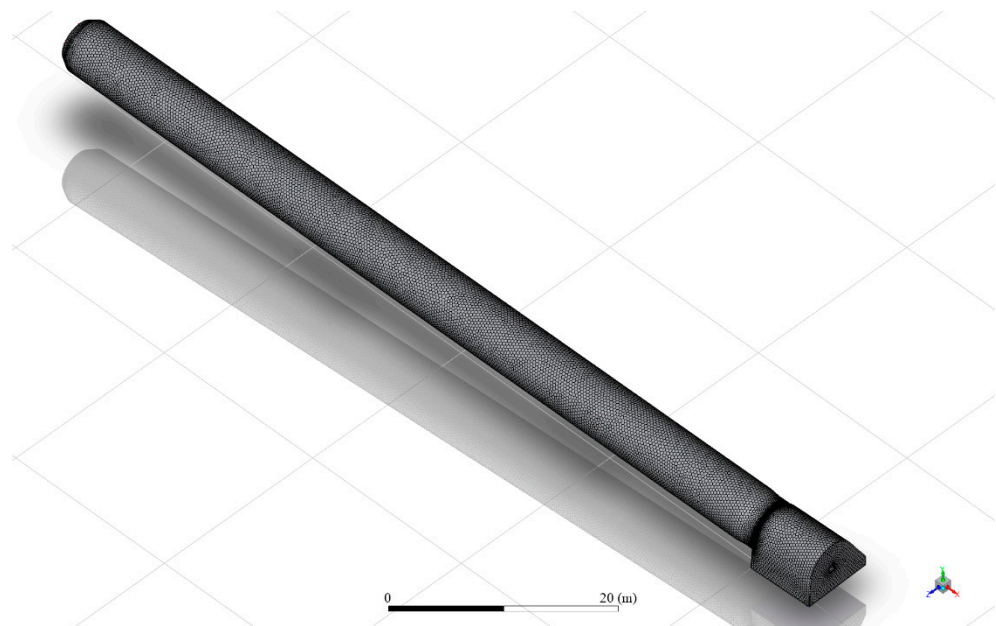


Figure 4. Meshed computational volume.

The volume was processed in Fluent Meshing, yielding a mesh with 1.2 million cells and a minimum orthogonal quality of 0.2, making it adequate for CFD simulation. Figure 5 shows a cut plane along the kiln length. The magnification focuses on the cooler hood and burner section, and it shows a poly-hexcore mesh, with inflation near the walls and a body of influence (BOI) in the flame area. The body of influence is an important technique to improve resolution in critical areas, thus helping convergence while simultaneously keeping computational demands to an optimal value. In this case, the BOI increases the resolution in the flame area, where the complex combustion phenomena occur.

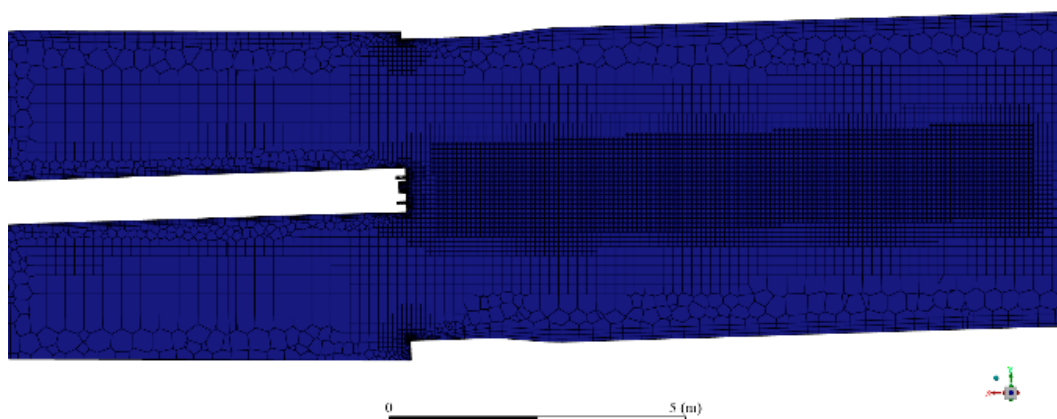


Figure 5. Mesh cut plane in the center of the kiln, highlighting the body of influence in the flame area.

2.2. Models

The turbulent flow field was modeled by employing the k - ω shear stress transport (SST) model [18,19]. This is one of the most well-established, state-of-the-art turbulence models, and it consists of two equations modeling the transport of turbulent kinetic energy and kinetic energy dissipation. Contrary to the standard k - ϵ model, it better models the fluid flow close to walls. It is particularly well suited to simulations at such a large scale as in the current work, keeping the computational demand under control for large mesh systems.

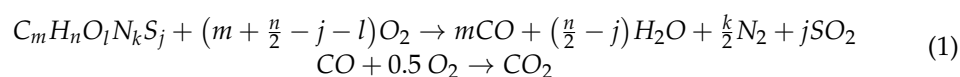
Radiative heat transfer was modeled using the Discrete Ordinates method [20,21], and the absorptivity of the flue gas mixture was modeled by the weighted sum of gray gases (WSSG) [22].

The combustion of solid fuels is a mixture of complex phenomena, with increasing complexity associated with multiple fuels. In the current model, fossil and alternative solid fuels were introduced as the main combustible species in the CFD domain. A combined Euler–Lagrange model was chosen to describe its behavior, where the gas phase is described by Euler equations, and the solid particles moving through the gas are described by the Lagrangian equation of motion. The two phases interact with each other, exchanging momentum, heat, and mass.

The behavior of the discrete phase is defined by a series of physical–chemical processes that begin as soon as the particle enters the domain. Firstly, the particle is heated up by contact with hot gases, releasing moisture in the form of water vapor. Then, a constant-rate devolatilization kinetic law defines the rate of gaseous volatile component release from the particle while simultaneously decreasing its diameter.

The fuel composition will thoroughly affect the combustion performance and is obtained from a combination of ultimate and proximate analyses. These define each of the fuels as a combination of ash, volatile matter, fixed carbon, and moisture.

The release of gaseous volatile components generates a model compound, $C_m H_n O_l N_k S_j$, whose subscripts are a result of the fuel analysis. Devolatilization was assumed to follow a constant-rate model. Gas phase combustion follows the oxidation of the volatile model compound according to:



where the reaction rate is calculated as the minimum between the turbulent mixing rate (R_t) and the Arrhenius kinetic rate law (R_k), as follows:

$$R_k = A e^{-E/(RT)} * \sum C_i^{m_i} \quad (2)$$

where A is the pre-exponential factor, E is the activation energy, and C_i is the concentration of reactant i to the power of m_i . The turbulent mixing rate is usually described by the Magnussen formula [23]:

$$R_t = A \frac{\rho_f}{M_{fu}} \frac{\epsilon}{k} \min \left(Y_{fu}, \frac{Y_{ox}}{\nu}, B \frac{\sum Y_{pr}}{1 + \nu} \right) \quad (3)$$

where A and B are the model coefficients and typically equal to 4 and 0.5, respectively. ϵ/k represents the inverse of the large-eddy mixing time scale, ρ_f is the density of the fluid, M_{fu} is the molar mass of the fuel, ν represents the kinematic viscosity, and Y_{fu} , Y_{ox} , and Y_{pr} represent the mass fractions of fuel, oxidant, and product species, respectively. The overall reaction rate is the minimum value between the turbulent mixing rate and finite-rate Arrhenius kinetic.

The gaseous volatile component will then combust, generating the expected combustion products and pollutants, while an additional model governs soot formation and subsequent combustion.

Pollutant generation is also considered, namely, SO_2 derived from the fuels' sulfur content and NO_x as a combined effect of fuel nitrogen and thermal mechanisms. The thermal NO_x model is a postprocessing calculation performed after combustion due to the low concentrations of NO_x in the combustion system, which means that NO_x chemistry usually exerts a negligible effect on the flow field. It follows the extended Zeldovich mechanism while simultaneously considering a N_2O intermediate compound and interaction with turbulence and species [24].



The kinetic constants for the reactions were obtained from a critical analysis of the literature data published by Hanson and Salimian [25]. The net rate of formation of NO is given by the following equation:

$$\frac{dNO}{dt} = k_{f,1}[O][N_2] + k_{f,2}[N][O_2] + k_{f,3}[N][OH] - k_{r,1}[NO][N] - k_{r,2}[O][NO] - k_{r,3}[H][NO] \quad (5)$$

Soot formation and combustion are solved by considering the one-step Khan and Greeves model [26], which details a single transport equation for the soot mass fraction as follows:

$$\frac{\partial}{\partial t}(\rho Y_{Soot}) + \nabla \cdot (\rho \vec{v} Y_{Soot}) = \nabla \cdot \left(\frac{\mu_t}{\sigma_{Soot}} \nabla Y_{Soot} \right) + R_{Soot} \quad (6)$$

where Y_{Soot} is the soot mass fraction, σ_{Soot} represents the turbulent Prandtl number for soot transport, and R_{Soot} represents the net rate of soot generation. The kinetics of soot combustion are given by the Magnussen and Hjertager model [23], according to:

$$R_1 = A \rho Y_{Soot} \frac{\epsilon}{k} \text{ or } R_2 = A \rho \left(\frac{Y_{OX}}{\nu_{Soot}} \right) \left(\frac{Y_{Soot} \nu_{Soot}}{Y_{Soot} \nu_{Soot} + Y_{fuel} \nu_{fuel}} \right) \frac{\epsilon}{k} \quad (7)$$

where A is a constant in the Magnussen model, Y_{OX} , Y_{fuel} are the mass fractions of the oxidizer and fuel, and ν_{Soot} , ν_{fuel} are the mass stoichiometries for soot and fuel combustion. Additionally, the rate of soot combustion is taken as the minimum value obtained between R_1 and R_2 .

Finally, heat loss at the kiln walls is modeled by a combination of convection and radiation boundary conditions.

2.3. Tested Scenarios

The CFD simulations performed for the kiln system are based on the principle of diagnosing the baseline operating conditions and attempting their optimization by fine-tuning operational parameters. Preliminary results suggest that there is not enough oxygen available for combustion in a critical area of the kiln (sintering zone), which prevents complete combustion from occurring. This was performed by calculating the excess air coefficients along the kiln and observing premature flame starvation, which was validated in the baseline simulation. Hence, in order to attempt the optimization of solid fuel combustion, the mass flow rate of secondary air was slightly increased to better aerate the oxygen-deprived flame. The fuel composition and all other relevant parameters were kept constant, with the purpose of isolating the effect of the additional secondary air mass flow rate.

Table 2 summarizes the differences in operating/boundary conditions for the two different simulations (see fuel specifications in Table 1). The simulations were run on a workstation with two 16-core intel Xeon CPUs and 256 GB of RAM. Convergence criteria are 10^{-4} in continuity, velocity, turbulence, and species (except NOx) and 10^{-6} in energy, radiation intensity, and NOx pollutant species. Additionally, the volume-average temperature needed to be stable. Convergence was reached after approximately 24 h.

Table 2. Boundary conditions for the CFD simulations.

Parameter	Baseline Case	Optimization Attempt
Petcoke flow rate (t/h)	3.0	3.0
RDF flow rate (t/h)	8.3	8.3
Axial air (Nm ³ /h)	4200	4200
Radial air (Nm ³ /h)	4300	4300
Petcoke transport air (Nm ³ /h)	2800	2800
RDF transport air (Nm ³ /h)	3000	3000
Secondary air (Nm ³ /h)	68,000	78,000

3. Results and Discussion

As previously mentioned, two case scenarios were simulated for the combustion process of petcoke and RDF within a rotary cement kiln.

3.1. Temperature and Velocity Profiles

Figures 6 and 7 show the average temperature and radial velocity, respectively. Since the axial distribution profiles are not easy to distinguish, Figure 8 shows the absolute difference between the two case scenarios for temperature, highlighting their main differences. Figure 9 shows the axial distribution fields along the rotary kiln, and, as previously, since the axial distribution profiles are not easy to distinguish, Figure 10 shows the absolute difference between the axial velocity distributions. These figures show the profiles starting from -81 m, with the location of the burner in the kiln at 0 m, which is the reference point for the injection of the raw meal.

Figure 6a shows that the overall temperature profile reaches slightly lower values when the secondary air mass flow rate increases. However, the temperature difference is not significant between the two cases, showing a maximum absolute difference of 74 °C at -65 m, which corresponds to deviations of 3.9% and 3.8% from the maximum temperature for the baseline and optimization case scenarios, respectively. Additionally, due to the higher secondary mass flow selected for the combustion optimization, the maximum temperature location is reached with a marginal delay of 0.7 m (approximately 0.9% of the kiln length) at -53 m. Hence, it can be inferred that the combustion process was not negatively affected. Observing Figures 7 and 8, it is possible to identify the body of the flames in the two case scenarios and the absolute difference between them, respectively. The area that denotes a higher absolute temperature difference intensity is observed between -73 m and -55 m, which corresponds to the main body of the flame location and kiln

walls. Similar temperature trends were observed in the works by Liedmann et al. [7], Pieper et al. [11], and Huang et al. [12].

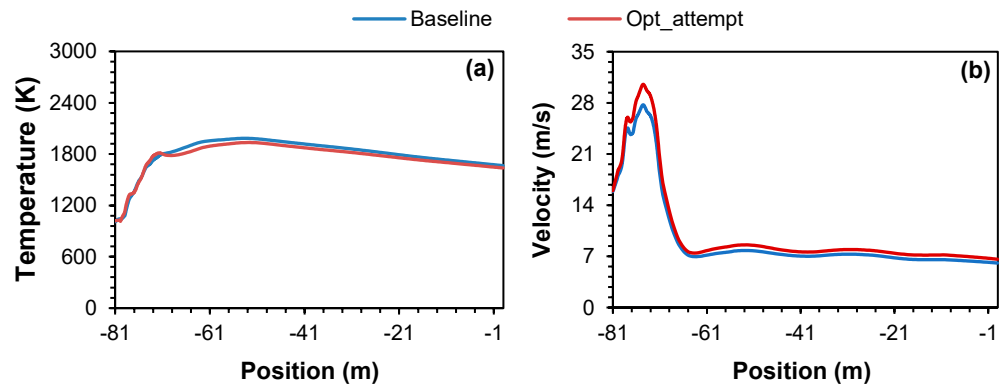


Figure 6. Average (a) temperature and (b) velocity values along the rotary kiln.

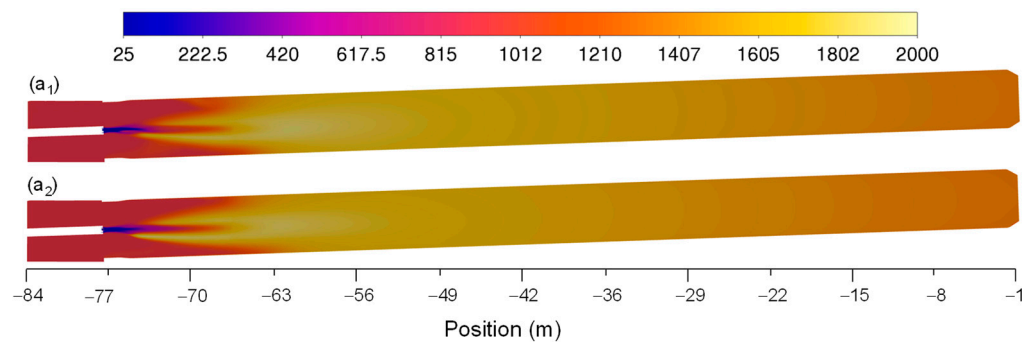


Figure 7. Baseline and optimization attempt case scenarios for axial temperature (a₁, a₂) distribution fields along the rotary kiln, respectively.

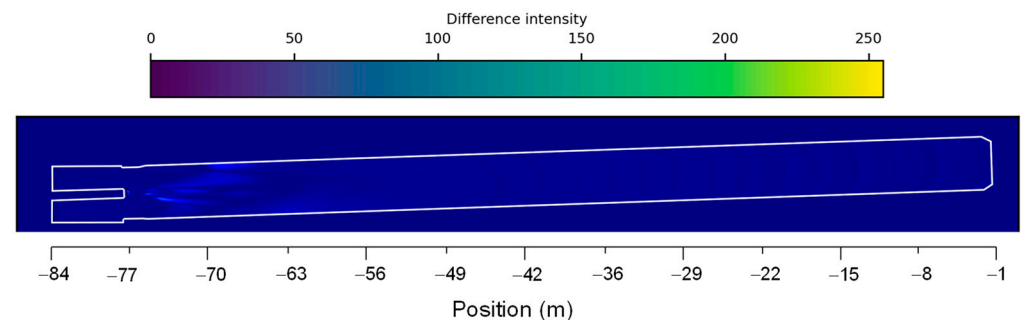


Figure 8. Absolute difference between the two case scenarios of the temperature distribution field along the rotary kiln.

Figure 6b shows that, as expected, the velocity profile reaches higher values when the secondary air mass flow rate increases, with the maximum absolute difference of 2.85 m/s located at -74 m. The flow velocity for both scenarios stabilizes to some degree at approximately -65 m, having small oscillations between 6 m/s and 8 m/s. Observing Figure 9, it is possible to identify that the flow reaches higher velocities in the area where the flame is located (higher-temperature location) for the two case scenarios. Similar to Figure 8, Figure 10 denotes that the higher absolute flow-velocity difference intensity is also observed between -75 m and -55 m, showing a greater difference located in the center of the flame and kiln walls. Similar flow velocity trends were also observed in previous works [7,11,12].

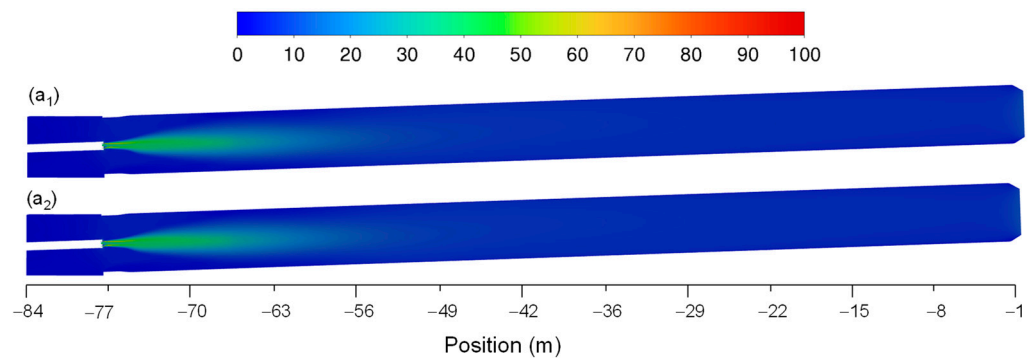


Figure 9. Baseline and optimization attempt case scenarios for axial velocity (a_1, a_2) distribution fields along the rotary kiln, respectively.

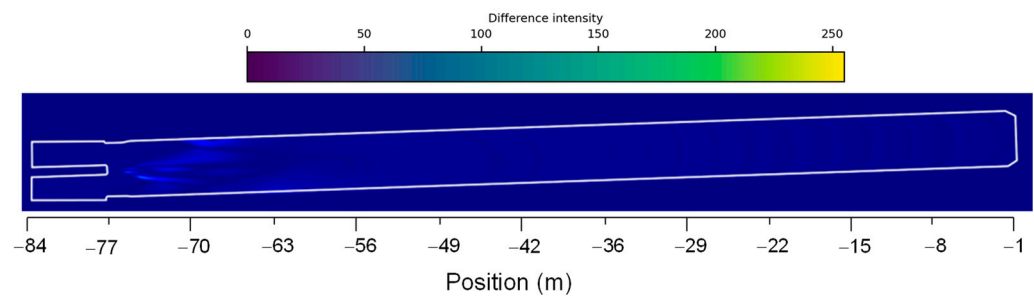


Figure 10. Absolute difference between the two case scenarios of velocity distribution fields along the rotary kiln.

Figure 11 shows the fluid flow path lines in baseline conditions, depicting both the kiln system (with magnification) and the primary air exiting the burner.

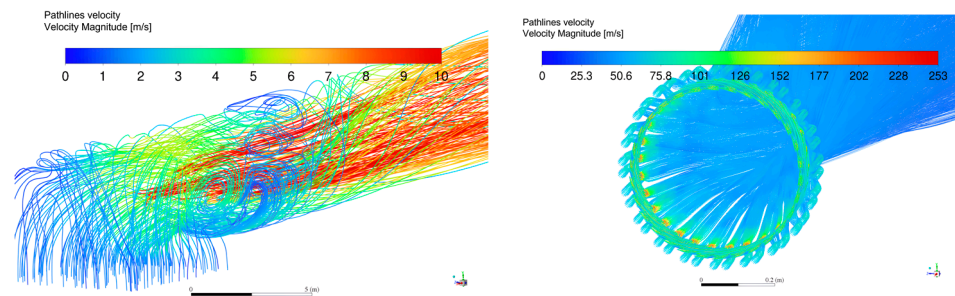


Figure 11. Velocity path lines for the magnified kiln (left) and burner (right) in baseline conditions.

The kiln path lines highlight the interaction between the secondary air and primary air, which happens due to the vastly different velocities. It is especially interesting to observe a slight recirculation zone, represented by the blue path lines adjacent to the red ones. This indicates that some material buildup might occur in the sintering zone of the kiln. The burner path lines highlight the strong swirl effect caused by the swirl air, which is depicted by the rotation of the path lines along the central axis. This strong swirl effect aids in flame control, particularly at the start of the flame, as afterward, the jets tend to separate and widen. Overall, the obtained path lines were very similar between the baseline and optimized conditions, and, as such, the path line images for the optimized conditions were omitted.

3.2. Chemical Species and Pollutants

Combustion is a fundamental process in the cement industry, where achieving a complete process is essential for maximizing energy efficiency and minimizing harmful emissions. When the fuels (petcoke and RDF, in the present case) burn in the presence of

oxygen, the combustion process typically results in the formation of CO₂ and H₂O vapor as primary by-products. However, the ratio of fuel to air can significantly impact the outcome of this thermal conversion process. In a lean combustion regime, a higher amount of oxidant facilitates a more thorough and efficient combustion process. The excess air allows for the complete oxidation of the fuel, resulting in a higher conversion of the fuel and the reduced formation of pollutants such as CO, soot, and unburned hydrocarbons [27]. These occurrences can be observed in Figures 12 and 14 and later in Table 3.

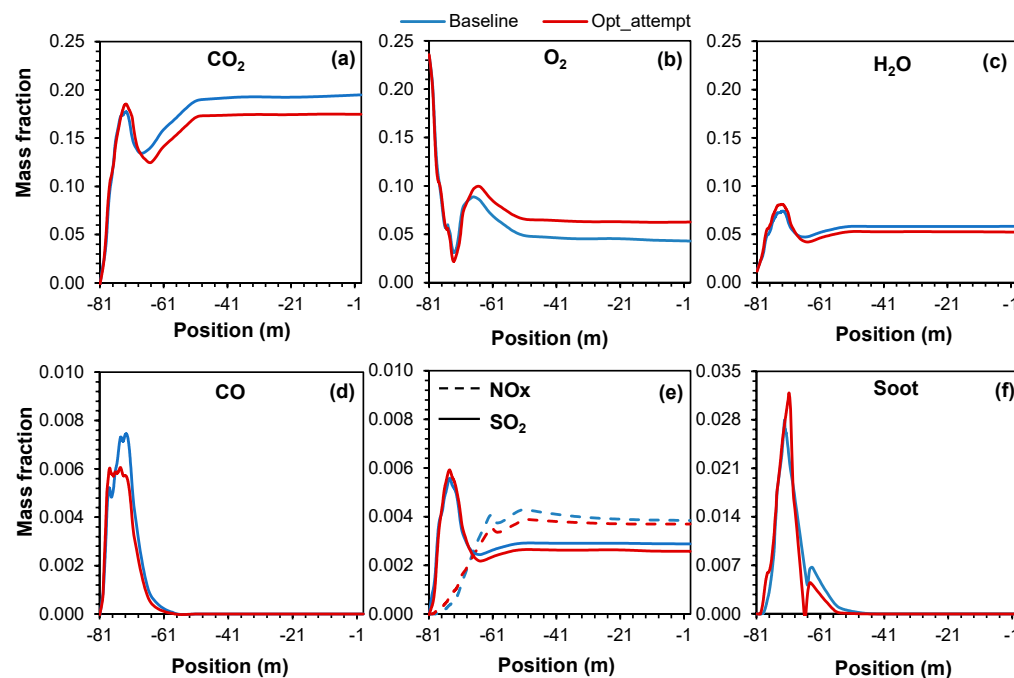


Figure 12. Axial distributions of mass fractions of (a) CO₂, (b) O₂, (c) H₂O, (d) CO, (e) NO_x, and (f) soot.

Table 3. Combustion process efficiency.

Fuel Inlet		
RDF mass flow (kg/s)		2.30
C _{RDF} (wt.%)		63.0 ^a
Petcoke mass flow (kg/s)		0.84
C _{Petcoke} (wt.%)		86.0 ^a
C mass flow (kg/s)		2.17
Outlet		
	Baseline	Optimization
Gas mass flow (kg/s)	32.72	36.09
CO ₂ yield (wt.%)	19.0	18.0
CO ₂ mass flow (kg/s)	6.33	6.55
C mass flow (kg/s)	2.01	2.09
Efficiency	92.95	96.20

^a Obtained from fuel elemental analysis.

Figure 12 shows the axial distributions of the mass fractions of the most important species (CO₂, O₂, H₂O, CO, SO₂, NO_x, and soot) during the combustion process regarding the two case scenarios.

Figure 12 shows that it is possible to distinguish two combustion stages. Initially, the increase in CO₂ (Figure 12a), H₂O (Figure 12c), and CO (Figure 12d) is primarily a result of fuel devolatilization, i.e., when in contact with a high temperature, the volatile matter present in the fuels starts to be immediately released and, due to the lack of O₂ (Figure 12b),

incomplete combustion occurs (also inherent to the presence of CO). Relating this phenomenon to Figures 6a and 7, it can be seen that between -81 m and -69 m, the body of the flame starts to form, and the temperature starts to increase. Immediately afterward, during the second stage of combustion, a further rise in CO_2 levels is observed. This phenomenon is attributed to the intense combustion of the remaining fuels and oxygen, where a greater amount of heat is released, leading to the formation of a localized high-temperature zone (flame area) at the center of the kiln (located between -69 m and -41 m). Finally, the consumption of oxygen reaches a state of stability, leading to a relative equilibrium in the levels of CO_2 , CO, H_2O , and the flow field (latter is also observed in Figure 9). These events were also observed in the work by Huang et al. [12]. Specifically comparing the results of the simulated case scenarios, when the air mass flow increases (making the mixture leaner), more oxygen is available to achieve complete combustion. Under these conditions, there is a more complete oxidation of the fuel, resulting in an initially slightly high production of CO_2 and H_2O vapor while, simultaneously, the production of O_2 and CO is further reduced. It is also important to note that air is composed of about 79% nitrogen (N_2) by volume. Because N_2 is generally an inert element in the combustion reaction, it will effectively dilute the concentration of the released gaseous species in the combustion products, decreasing their concentration in the exhaust gases, as observed in Figure 12a–d. Additionally, although nitrogen is mostly inert, at high temperatures (above ~ 1800 K), oxygen and nitrogen can react to form various nitrogen oxides (NOx). High temperature is a key factor that contributes to the formation of NOx [27]. This phenomenon can be observed in relation to Figures 6, 7 and 12e. Overall, the higher concentration of NOx is located in the area where the temperature is higher (center of the flame), and, additionally, the case scenario with a higher temperature (less available air) results in higher NOx emissions, which is more apparent at -61 m in Figure 12e. Similar results were also observed by Huang et al. [12].

SO_2 emissions primarily rely on the sulfur content within the fuel rather than the combustion regime. Regardless of whether the combustion conditions are lean or rich, sulfur is nearly entirely oxidized to SO_2 during the combustion process. Therefore, altering the air–fuel ratio by augmenting the air mass flow would have a minimal impact on the quantity of SO_2 generated, assuming that the sulfur content in the fuels remains constant [27]. Nonetheless, the concentration of SO_2 in the flue gas could be lower under lean conditions, similar to the situation with the other released gaseous species, owing to the dilution effect resulting from the increased amount of nitrogen and other inert components in the excess air. The dilution effect is observed in Figure 12e.

The formation of soot, or particulate matter, is primarily influenced by the composition of the fuels and the equivalence ratio during combustion. Under lean combustion conditions, where the air mass flow is increased, the formation of soot tends to decrease. This is due to the more oxygen available to oxidize the fuels completely to CO_2 and H_2O vapor, reducing the formation of partially oxidized hydrocarbons and carbon particles. Also, the excess air can oxidize any soot particles that are produced, further reducing soot emissions. Figure 12b,f show the described relation between O_2 and soot particle formation.

Figure 13 shows the absolute difference between the two case scenarios of CO_2 , O_2 , H_2O , CO, NOx, and soot distribution fields along the rotary kiln. Since the formation of SO_2 depends mainly on the composition of the fuels [27], the discussion of this species was considered not relevant to this topic. Differently from what was observed for the temperature and velocity distribution fields (Figures 8 and 10), and regardless of being located in the flame region, there are two defined areas that denote a higher absolute difference intensity, approximately separated at -69 m. Relating this event to Figure 12, this region corresponds not only to where both case scenarios present similar results but also to the region that separates the two combustion stages. In the region of the first combustion stage, the absolute difference intensity corresponds to the lower formation of CO (where partial combustion occurs), higher consumption of O_2 , and higher production of CO_2 , H_2O , and soot in the case scenario where the air mass flow was increased, whereas in the region of the second combustion regime, the opposite trends are observed. Additionally,

it is also possible to observe that complete combustion occurs, which can be easily related to the differences detected mostly in the production of CO_2 and soot and their absence in the production of CO . Regarding Figure 13e, since the temperature is generally lower for the referred case scenario, the absolute difference intensity corresponds to the lower formation of NO_x . Once again, it is also curious to observe the inverse relationship between O_2 (Figure 13b) and soot (Figure 13f) formation. The regions lacking oxygen correspond to the regions where the production of soot increases.

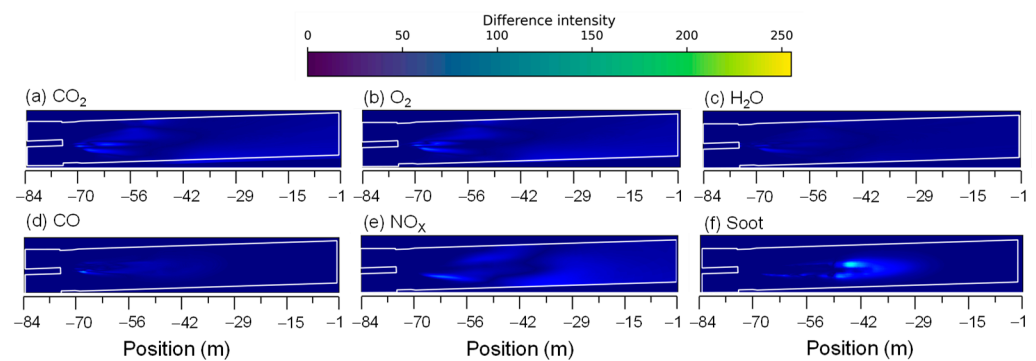


Figure 13. Absolute differences in (a) CO_2 , (b) O_2 , (c) H_2O , (d) CO , (e) NO_x , and (f) soot distribution fields along the rotary kiln between the two case scenarios.

3.3. Solid Fuel Combustion and Combustion Efficiency

Particle burnout refers to the complete combustion of solid fuel particles, leaving no unburned material behind. This parameter represents a crucial aspect of combustion systems, ensuring maximum energy efficiency and minimal emissions [27]. Figure 14 shows the axial distributions of the burnout rate of petcoke and RDF particles.

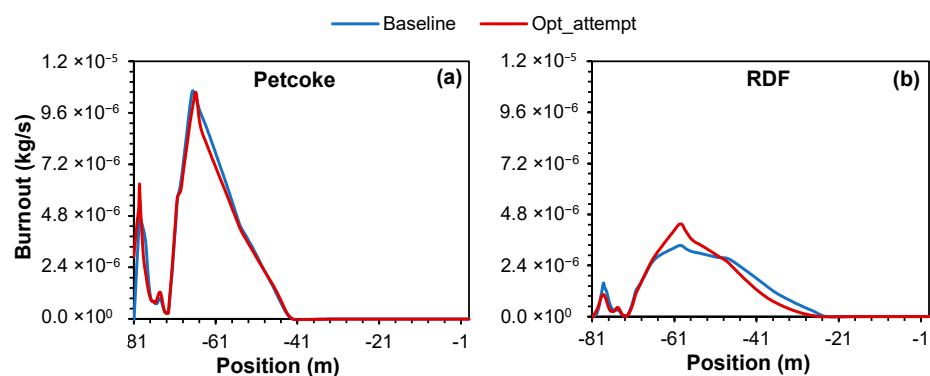


Figure 14. Axial distributions of the burnout rate of (a) petcoke and (b) RDF particles.

In the case of petcoke particles (Figure 14a), it can be inferred that the increase in the air mass flow had little effect on the burnout, meaning that the combustion process of petcoke particles was marginally affected, regardless of the slight decrease in the temperature at around -61 m. On the other hand, in the case of RDF particles (Figure 14b), the excess air ensures a more efficient oxidation of the fuel particles, resulting in a higher and faster conversion of the fuel into gaseous combustion products. This leads to improved energy efficiency and reduced emissions of unburned materials and pollutants by facilitating the breakdown of complex fuel molecules and promoting the complete oxidation of solid particles. The reason that petcoke burnout ends before RDF burnout (around -41 m and -30 m, respectively) is primarily due to its higher thermal conductivity and heat content and due to the smaller particle size. Hence, when subject to a high temperature, petcoke will start to decompose and react faster than RDF. Similar results were observed in the works by Pieper et al. [11] and Ariyaratne et al. [14].

Table 3 shows the combustion process efficiency for the two simulated case scenarios. It is possible to conclude, for the tested conditions, that increasing the air mass flow by 10% improved the carbon conversion efficiency by 3.25%. As a result, a lean combustion regime can lead to a higher combustion efficiency as more of the fuel is oxidized. However, this must be balanced against the possibility of increasing emissions of NO_x and potential impacts on the combustion operating conditions. Hence, there must be a balance between achieving efficient combustion, minimizing harmful emissions, and maintaining the reliability and performance of the combustion system.

4. Conclusions

The findings of this investigation into the operation of a real cement plant's rotary kiln system provide valuable insights for optimizing the combustion efficiency and pollutant emissions from cement production. The CFD model developed presented a high level of agreement with plant information, such as the flame temperature and the temperature at the end of the kiln. Furthermore, the baseline operating conditions were verified to yield low-oxygen conditions (flame starvation) at a relatively early stage in the gas flow.

The strategy for increasing the secondary air flow rate was thus confirmed, and the results obtained in the simulation confirm not only an improvement in burning conditions and flame behavior but also an increase in combustion efficiency from 93% to 96%, combined with a slight decrease in the pollutant mass fraction in the flue gas. This increase in combustion efficiency was a result of better flame aeration, which resulted in a direct improvement in RDF burnout.

Furthermore, no change was observed in the petcoke burnout, thus indicating that fossil fuel combustion is already optimal in the proposed conditions. The temperature and velocity profiles remained stable throughout the simulations and consistent with the information provided by plant operators.

Overall, the proposed CFD model is a powerful tool for the operational investigation and diagnosis of a complex system whose direct measurement is either impractical or even impossible, depending on the variables. Further model improvements can include a model for estimating the heat of reaction from clinkerization reactions, which can help improve the estimated temperature profiles along the kiln length.

Author Contributions: Conceptualization, D.M.C. and A.I.F.; methodology, D.M.C.; software, M.M.; validation, D.M.C. and A.I.F.; formal analysis, D.M.C. and A.I.F.; investigation, D.M.C.; resources, M.M.; data curation, D.M.C.; writing—original draft preparation, D.M.C. and A.I.F.; writing—review and editing, D.M.C. and A.I.F.; visualization, D.M.C. and A.I.F.; supervision, M.M.; project administration, M.M.; funding acquisition, M.M. All authors have read and agreed to the published version of the manuscript.

Funding: The authors acknowledge the funding of the P2020 Clean Cement Line project (LISBOA-01-0247-FEDER-027500). A.I. Ferreiro acknowledges Fundação para a Ciência e a Tecnologia (FCT) through IDMEC under LAETA, project UIDB/50022/2020.

Data Availability Statement: The data are not publicly available due to confidentiality.

Conflicts of Interest: The authors declare no conflict of interest.

References

1. Khoshnava, S.M.; Rostami, R.; Zin, R.M.; Kamyab, H.; Majid, M.Z.A.; Yousefpour, A.; Mardani, A. Green Efforts to Link the Economy and Infrastructure Strategies in the Context of Sustainable Development. *Energy* **2020**, *193*, 116759. [CrossRef]
2. Directorate-General for Climate Action European Climate Law. Available online: <https://climate.ec.europa.eu/> (accessed on 18 April 2023).
3. Kahawalage, A.C.; Melaaen, M.C.; Tokheim, L.-A. Opportunities and Challenges of Using SRF as an Alternative Fuel in the Cement Industry. *Clean. Waste Syst.* **2023**, *4*, 100072. [CrossRef]
4. Antunes, M.; Santos, R.L.; Pereira, J.; Rocha, P.; Horta, R.B.; Colaço, R. Alternative Clinker Technologies for Reducing Carbon Emissions in Cement Industry: A Critical Review. *Materials* **2022**, *15*, 209. [CrossRef]

5. Sharma, P.; Sheth, P.N.; Mohapatra, B.N. Recent Progress in Refuse Derived Fuel (RDF) Co-Processing in Cement Production: Direct Firing in Kiln/Calcliner vs. Process Integration of RDF Gasification. *Waste Biomass Valorization* **2022**, *13*, 4347–4374. [[CrossRef](#)]
6. Rahman, A.; Rasul, M.G.; Khan, M.M.K.; Sharma, S.C. Assessment of Energy Performance and Emission Control Using Alternative Fuels in Cement Industry through a Process Model. *Energies* **2017**, *10*, 1996. [[CrossRef](#)]
7. Liedmann, B.; Wirtz, S.; Scherer, V.; Krüger, B. Numerical Study on the Influence of Operational Settings on Refuse Derived Fuel Co-Firing in Cement Rotary Kilns. *Energy Procedia* **2017**, *120*, 254–261. [[CrossRef](#)]
8. Hemidat, S.; Saidan, M.; Al-Zu'bi, S.; Irshidat, M.; Nassour, A.; Nelles, M. Potential Utilization of RDF as an Alternative Fuel to Be Used in Cement Industry in Jordan. *Sustainability* **2019**, *11*, 5819. [[CrossRef](#)]
9. Wojtacha-Rychter, K.; Smoliński, A. Multi-Case Study on Environmental and Economic Benefits through Co-Burning Refuse-Derived Fuels and Sewage Sludge in Cement Industry. *Materials* **2022**, *15*, 4176. [[CrossRef](#)]
10. Liedmann, B.; Arnold, W.; Krüger, B.; Becker, A.; Krusch, S.; Wirtz, S.; Scherer, V. An Approach to Model the Thermal Conversion and Flight Behaviour of Refuse Derived Fuel. *Fuel* **2017**, *200*, 252–271. [[CrossRef](#)]
11. Pieper, C.; Liedmann, B.; Wirtz, S.; Scherer, V.; Bodendiek, N.; Schaefer, S. Interaction of the Combustion of Refuse Derived Fuel with the Clinker Bed in Rotary Cement Kilns: A Numerical Study. *Fuel* **2020**, *266*, 117048. [[CrossRef](#)]
12. Huang, Y.; Guan, J.; Kao, H. Numerical Simulation of Pulverized Coal Combustion in Rotary Kilns with Different Oxygen Concentrations. *Energy Sources Part A Recovery Util. Environ. Eff.* **2022**, *44*, 4510–4524. [[CrossRef](#)]
13. Pieper, C.; Wirtz, S.; Schaefer, S.; Scherer, V. Numerical Investigation of the Impact of Coating Layers on RDF Combustion and Clinker Properties in Rotary Cement Kilns. *Fuel* **2021**, *283*, 118951. [[CrossRef](#)]
14. Ariyaratne, W.K.H.; Malagalage, A.; Melaaen, M.C.; Tokheim, L.-A. CFD Modelling of Meat and Bone Meal Combustion in a Cement Rotary Kiln—Investigation of Fuel Particle Size and Fuel Feeding Position Impacts. *Chem. Eng. Sci.* **2015**, *123*, 596–608. [[CrossRef](#)]
15. Ryan, J.; Bussmann, M.; DeMartini, N. CFD Modelling of Calcination in a Rotary Lime Kiln. *Processes* **2022**, *10*, 1516. [[CrossRef](#)]
16. Mikulčić, H.; Cerinski, D.; Baleta, J.; Wang, X. Improving Pulverized Coal and Biomass Co-Combustion in a Cement Rotary Kiln by Computational Fluid Dynamics. *Chem. Eng. Technol.* **2019**, *42*, 2539–2545. [[CrossRef](#)]
17. Lahaye, D.; Juretić, F.; Talice, M. Modelling a Turbulent Non-Premixed Combustion in a Full-Scale Rotary Cement Kiln Using ReactingFoam. *Energies* **2022**, *15*, 9618. [[CrossRef](#)]
18. Menter, F. Zonal Two Equation K- ω Turbulence Models For Aerodynamic Flows. In Proceedings of the 23rd Fluid Dynamics, Plasmadynamics, and Lasers Conference, Nashville, TN, USA, 6–8 July 1992; American Institute of Aeronautics and Astronautics: Reston, VA, USA, 1992.
19. Menter, F.R. Two-Equation Eddy-Viscosity Turbulence Models for Engineering Applications. *AIAA J.* **1994**, *32*, 1598–1605. [[CrossRef](#)]
20. Raithby, G.D.; Chui, E.H. A Finite-Volume Method for Predicting a Radiant Heat Transfer in Enclosures with Participating Media. *J. Heat Transf.* **1990**, *112*, 415–423. [[CrossRef](#)]
21. Chui, E.H.; Raithby, G.D. Computation of Radiant Heat Transfer on a Nonorthogonal Mesh Using the Finite-Volume Method. *Numer. Heat Transf. Part B Fundam.* **1993**, *23*, 269–288. [[CrossRef](#)]
22. Hottel, H.C.; Sarofim, A.F. *Radiative Transfer*; McGraw-Hill: New York, NY, USA, 1967.
23. Magnussen, B.F.; Hjertager, B.H. On Mathematical Modeling of Turbulent Combustion with Special Emphasis on Soot Formation and Combustion. *Symp. (Int.) Combust.* **1977**, *16*, 719–729. [[CrossRef](#)]
24. The Oxidation of Nitrogen in Combustion and Explosions. In *Selected Works of Yakov Borisovich Zeldovich*; Princeton University Press: Princeton, NJ, USA, 2014; Volume 1, pp. 364–403, ISBN 978-1-4008-6297-9.
25. Hanson, R.K.; Salimian, S. Survey of Rate Constants in the N/H/O System. In *Combustion Chemistry*; Gardiner, W.C., Ed.; Springer: New York, NY, USA, 1984; pp. 361–421, ISBN 978-1-4684-0186-8.
26. Khan, I.; Greeves, G. A Method for Calculating the Formation and Combustion of Soot in Diesel Engines. *Heat Transf. Flames* **1974**, *25*, 389–404.
27. Turns, S.R. *An Introduction to Combustion: Concepts and Applications*, 3rd ed.; McGraw-Hill: New York, NY, USA, 2011; Volume 1, ISBN 978-0-07-338019-3.

Disclaimer/Publisher's Note: The statements, opinions and data contained in all publications are solely those of the individual author(s) and contributor(s) and not of MDPI and/or the editor(s). MDPI and/or the editor(s) disclaim responsibility for any injury to people or property resulting from any ideas, methods, instructions or products referred to in the content.